AIAA JOURNAL
Vol. 43, No. 5, May 2005

Large-Structure Topology in a Three-Dimensional Supersonic Base Flow

Alan L. Kastengren* and J. Craig Dutton†
University of Illinois at Urbana–Champaign, Urbana, Illinois 61801

The near wake of a blunt-base cylinder at 10-deg angle of attack to a Mach 2.46 freestream flow is studied using Mie scattering flow visualization. Large-scale structures are clearly evident in side-view images of the windward and lateral parts of the shear layer but not in the leeward shear layer. Autocorrelation analysis shows that the average structures grow substantially in side views as the shear layer develops on the lateral plane and the windward shear layer, but not the leeward shear layer. End-view images show that a septum originates from the leeward part of the shear layer and extends to the windward part of the shear layer during reattachment, dividing the wake into two lobes after reattachment and causing a short reattachment length. The structures in end-view images are largest in the windward part of the shear layer and increase in size as the shear layer develops. The structures are inclined toward the leeward direction in the lateral plane, indicating circumferential flow from windward to leeward in the main shear layer. The appearance of the images suggests that this circumferential flow causes mass buildup on the leeward side of the wake, prompting the formation of the septum.

I. Introduction

COMPRESSIBLE turbulent shear layers have been a subject of research interest for many years. It is well established that compressibility effects, as measured by the convective Mach number M_c, can strongly affect the structure of shear layers. For example, in planar mixing layers, compressibility effects reduce the shear layer growth rate[1,2] and suppress turbulent fluctuations in the shear layer.[3,4] Moreover, compressibility significantly alters the appearance of the large-scale coherent structures found in the shear layer. For low M_c, the large-scale structures appear as well-organized two-dimensional spanwise rollers, similar to those found in incompressible mixing layers.[5] For $M_c > 0.6$, the structures appear much less organized, with a more three-dimensional topology.[2]

The study of large-scale coherent structures in base flows is particularly important. First, the development of large-scale structures in base flow shear layers helps determine the rate of entrainment of fluid out of the recirculation region.[6] This, in turn, establishes the base pressure and base drag. As opposed to simple planar shear layers, compressible base flow shear layers encounter many regions with extra rates of strain,[7] including expansion at separation, streamline curvature and convergence near reattachment, and recompression during reattachment. These effects have been shown in previous studies[8–10] to alter significantly the appearance of coherent structures in compressible flows.

The literature on large-scale coherent structures in compressible base flows is rather limited. Smith and Dutton[11] described the large-scale structures in a compressible planar base flow, whereas Bourdon and Dutton[12] described the large-scale structures in an axisymmetric blunt base flow at $M = 2.46$. With the use of planar Mie scattering imaging, these studies found that the large-scale structures were on average elliptical and inclined to the freestream flow in side-view images in both cases, matching the results from planar mixing layer studies.[13] Because of the high convective Mach number of the shear layers, the structures were not regularly spaced and often had a jagged appearance in instantaneous images. In side-view images, the structures grew markedly and became more elongated during recompression and reattachment, whereas the structures became more disorganized in appearance in the instantaneous images. In end-view images, both studies found mushroom-shaped large-scale structures, which matches the results for incompressible mixing layers.[5] Scarano and van Oudheusden,[14] as part of a particle image velocimetry study of a planar base flow at $M = 2.0$, found large-scale coherent structures in vorticity data for the trailing wake, with the structure sizes ranging from 17 to 50% of the local half-width of the wake. Other data for large-scale coherent structures in supersonic base flows appear to be lacking.

In the current study, the topology of the wake of a blunt-base cylinder at 10-deg angle of attack to a supersonic freestream flow is investigated. This geometry may be encountered by missiles and projectiles in parts of their mission profile. Also, this body presents a generic three-dimensional wake for study, as opposed to the planar and axisymmetric geometries studied to date. The literature for three-dimensional supersonic blunt-body wakes is very limited. Boswell and Dutton have previously studied the velocity field and afterbody pressure distribution for the current flowfield.[15–17] They found a thick boundary layer on the lee side of the afterbody and circumferential flow around the afterbody from the windward to leeward sides. A large pressure difference, amounting to 70% of the freestream static pressure, was noted between the leeward and windward planes of the afterbody at separation. Strong radial flow from leeward to windward was also noted in the near wake, as was a bifurcated wake and a short reattachment length. The measured base pressure normalized by the freestream static pressure was 48% lower than that for a corresponding axisymmetric base flow. Literature on large-scale structures in three-dimensional blunt-body wake shear layers appears to be lacking.

The current paper addresses the topology of the large-scale coherent structures in the shear layer for this three-dimensional separated flow. These data will be compared to the axisymmetric blunt-base data by Bourdon and Dutton,[12] to show how the three-dimensional nature of the flow impacts the structure of the shear layer. The visualizations will be used in conjunction with previously obtained mean velocity and turbulent stress data[16,17] for this flow to better characterize the structure of the wake. The current flow lacks the symmetry of the previously cited planar and axisymmetric flows, so that much more effort is required to understand the dynamics of the wake.

Received 7 May 2004; presented as Paper 2004-2340 at the AIAA 34th Fluid Dynamics Conference, Portland, OR, 28 June–1 July 2004; revision received 18 October 2004; accepted for publication 18 October 2004.

*NDSEG Fellow, Department of Mechanical and Industrial Engineering, 1206 West Green Street. Student Member AIAA.

†Donald Biggar Willet Professor, Department of Mechanical and Industrial Engineering, 1206 West Greet Street. Associate Fellow AIAA.

II. Experimental Equipment and Techniques

The flow facility used in this work is an intermittent blowdown supersonic wind tunnel with an annular converging–diverging (C–D) nozzle, allowing base flow models to be supported from upstream via a sting. The upstream support prevents the interference effects that side or rear supports would introduce. These interference effects have been shown to alter significantly the structure of supersonic base-flow wakes.[18] The nozzle exit diameter for this facility is 144 mm. The approaching freestream Mach number is 2.46 (Ref. 19), with a unit Reynolds number of 56×10^6/m. Other important flow parameters are given in Table 1.

The afterbody in this study is a cylinder 63.5 mm in diameter, with a sudden 10-deg bend. The length-to-radius ratio after the bend is 3.0. A schematic of the afterbody and some nomenclature for the following discussion are given in Fig. 1. The length of the afterbody has been chosen so that the waves originating from the junction between the support sting and the afterbody reflect onto the wake downstream of the area studied in this investigation and downstream of the point where the wake has reaccelerated to supersonic speeds. This has been confirmed by visualizations of the flow. Hence, interference effects from these reflected waves are not deemed important in the present study. Figure 2 shows the geometry of the flow facility, the position of the afterbody in the flow facility, and the behavior of the reflected waves from the sting–afterbody junction.

Passive scalar Mie scattering is used to visualize this flow. This technique allows instantaneous two-dimensional visualization of the flow and does not suffer from the spatial integration effects inherent to schlieren and shadowgraph imaging. The technique has been used by many investigators to study large-scale structures in compressible shear layers.[2,8,10–12,20] The flow is seeded far upstream with a small amount of a volatile liquid (ethanol in this study). The liquid evaporates and mixes with the supply air before reaching the tunnel stagnation chamber. On expansion in the C–D nozzle, the vapor condenses as a uniform fog of droplets. Phase equilibrium allows liquid droplets to remain stable in supersonic regions of the flow, but in warmer, subsonic regions, the droplets evaporate. The mean droplet diameter as estimated by previous investigators is roughly 50 nm (Ref. 20) which allows the particles to respond accurately to changes in the velocity and static temperature of the flow.[21,22]

The droplets are visualized by light scattering. A planar sheet of laser light 750 ± 100 μm thick is directed through the flow, illuminating a thin cross section. The droplets scatter this light, and an unintensified 16-bit charge-coupled device camera records the scattered light intensity. The laser is a pulsed, frequency-doubled Nd:YAG laser, with a pulse duration of 6–8 ns. Hence, the images are very well time resolved, that is, unsmeared. The time between successive images is 0.2–0.4 s, and so successive images are uncorrelated in time. Typical laser energy values are 30–100 mJ per pulse.

Note that the behavior of the alcohol droplets for Mie scattering depends on the static pressure, temperature, and density of the flow. Hence, this technique is qualitative in nature. This technique has been successful in capturing the dynamics of coherent structures in a wide range of compressible flows. However, care must be taken in comparing the appearance of structures from areas in the flow with significantly different thermodynamic conditions, such as areas separated by wide distances or on opposite sides of shock waves.

Three kinds of images are obtained. First, side-view images of the shear layer in the lateral and symmetry planes of the wake are obtained. Diagrams of these imaging locations are given in Figs. 3 and 4. Second, global end-view images of the entire wake are gathered at several axial locations in the wake. Third, detailed end-view images of smaller areas of the developing shear layer are obtained for axial positions before reattachment. Important imaging parameters are given in Tables 2 and 3.

The most important contributor to noise in the images is laser speckle.[23,24] This noise is an interference effect that occurs when coherent light strikes a diffuse reflector, such as the Mie scattering droplets. It can be reduced by using collecting optics with a

Table 1 Important freestream flow parameters

Parameter	Value
M_∞	2.46
T_∞	302 ± 2 K
P_∞	545 kPa $\pm$ 3%
Re_∞	56.4×10^6/m
Seeding	0.1–0.2% ethanol by mass

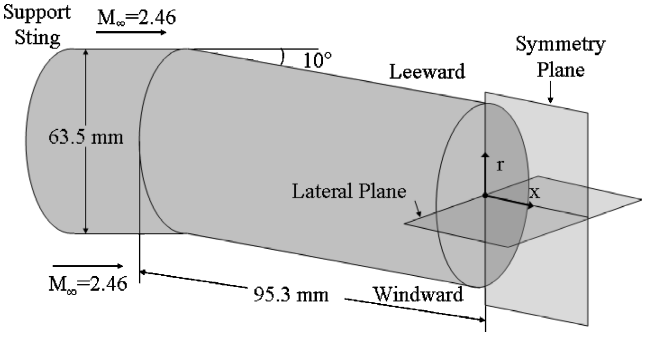

Fig. 1 Detail of afterbody geometry.

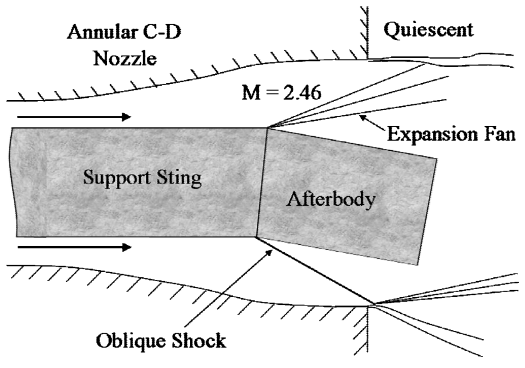

Fig. 2 Flow facility, afterbody position, and wave reflections.

Table 2 Side-view imaging parameters

Area	Distance from separation x/R	Image size, mm	M_c
Lateral A	0.48	$15.0 \times 15.0 \pm 0.2$	1.03
Lateral B	0.95	25.0×25.0	1.20
Lateral C	1.65	15.4×15.4	1.03
Lateral C septum	1.65	15.0×15.0	0.48
Lateral D	1.96	25.0×25.0	0.93
Lateral E	2.57	28.1×28.1	0.69
Leeward F	0.4	13.3×13.3	
Leeward G	0.7	13.3×13.3	
Leeward H	0.9	13.3×13.3	
Windward I	0.3	13.2×13.2	1.14
Windward J	0.6	13.2×13.2	1.31
Windward K	0.9	13.2×13.2	1.37
Wake L	1.7	25.1×25.1	
Wake M	2.3	25.1×25.1	

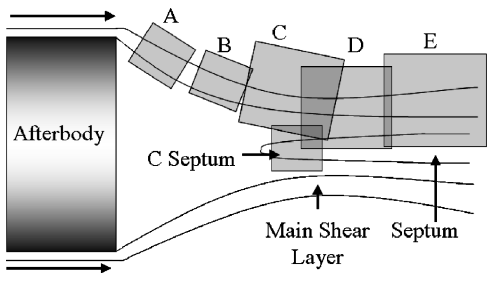

Fig. 3 Imaging locations schematic, lateral plane.

Table 3 End-view imaging parameters

Global images		Detailed images		
Distance from separation x/R	Image size, mm	Windward image size, mm	Lateral image size, mm	Leeward image size, mm
0.3	$91.3 \times 73.7 \pm 1.0$	$11.3 \times 13.4 \pm 0.2$	6.7×11.0	11.0×13.4
0.6	87.4×68.3	11.0×13.4	6.7×11.0	11.0×13.4
0.9	82.3×69.6	13.2×15.3	13.2×11.2	13.2×15.3
1.2	76.8×64.0			
1.6	70.6×60.0			
2.0	70.6×60.0			

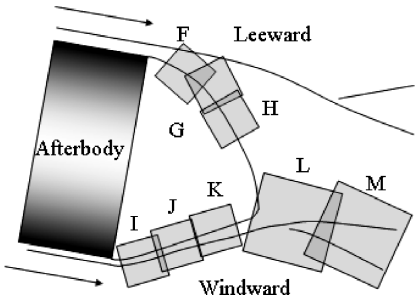

Fig. 4 Imaging locations schematic, symmetry plane.

large aperture. The side-view images presented are gathered using an equivalent aperture of $\ell/4$. Because of the geometry of the flow facility, true end-view images could not be obtained. For these images, the laser sheet is directed parallel to the base surface, but the camera images the scattered light at an oblique angle. Depth-of-focus requirements cause the aperture to be reduced to $\ell/16$. Thus, the end-view images have far more speckle noise, which is noticeable in the example images to follow.

A. General Image-Processing Techniques

At each imaging location, 640–1200 individual images are obtained. For all images, the background intensity is subtracted, using an image obtained with the laser on but the test section quiescent. Next, to eliminate large droplets from the images, isolated saturated pixels in the image are removed. If the image contains too many saturated pixels, is too dim, or has an atypical intensity distribution in the freestream, the image is rejected. The uniform freestream is used to correct for average intensity variations in the laser sheet. After these acceptance criteria are applied, 500–750 images typically remain for further processing. Routines are also applied to remove the perspective distortion from the end-view images.

B. Side-View Image Processing

The topology of the large-scale coherent structures is found via autocorrelation analysis. This technique has been used by several authors to study large-scale structures.[10–13,25] It is objective and relatively simple to implement. The extent over which high correlation values can be found gives an indication of the average topology of the large-scale coherent structures. The autocorrelation is calculated using the formulas given by Miles and Lempert[25]:

$$\tilde{I}_i(x, y) = I_i(x, y) - \frac{1}{n} \times \sum_n I_i(x, y) \tag{1}$$

$$I'(x, y) = \sqrt{\frac{1}{n} \times \sum_n [\tilde{I}_i(x, y)]^2} \tag{2}$$

$$\xi(x_0, \Delta x, y_0, \Delta y) = \frac{\sum_n \tilde{I}_i(x_0, y_0) \times \tilde{I}_i(x_0 + \Delta x, y_0 + \Delta y)}{n \times I'(x_0, y_0) \times I'(x_0 + \Delta x, y_0 + \Delta y)} \tag{3}$$

Here, n is the number of images in the ensemble, $I_i(x, y)$ is the intensity at (x, y) for image i, $\tilde{I}_i(x, y)$ is the instantaneous fluctuating intensity, $I'(x, y)$ is the rms of the fluctuating intensity, and $\xi(x_0, \Delta x, y_0, \Delta y)$ is the autocorrelation for a basis point (x_0, y_0) at a displacement $(\Delta x, \Delta y)$ from the basis point. For the side-view images, 11 basis points are used, all placed on the central column of the image spanning the middle-half of the mean shear layer thickness. The autocorrelation fields from the different basis points are averaged to give the final contours.

To determine the structure topology, the 0.6 correlation contour is defined as the outer edge of the average large-scale coherent structure. These contours are typically elliptical; to describe them quantitatively, an ellipse is fit to the contour, using the procedure outlined by Halíř and Flusser.[26] Structure size is defined as the major axis length of the fitted ellipse. The inclination angle is defined as the angle between the major axis of the fitted ellipse and the main shear layer direction. The eccentricity is defined as $e = (1 - b/a)$, where b is the semiminor axis length and a is the semimajor axis length. This matches the definition used by previous authors.[11,12]

Note that autocorrelation analysis gives a depiction of an average turbulent structure. Given the wide variety of shapes and sizes that the large-scale structures can assume, this average structure will not necessarily resemble a given instantaneous visualization of a structure. Nevertheless, the analysis will give a quantitative indication of how large the structures tend to be, how they tend to be shaped, and how they are typically oriented with respect to the mean shear layer.

C. End-View Image Processing

The autocorrelation analysis for the global end-view images is in principle the same as for the side-view images. For images up to reattachment, five basis points, spanning the middle-half of the shear layer, are placed on the windward, leeward, and lateral parts of the wake. After reattachment, the windward and leeward planes no longer have well-defined shear layers, but the septum is now present. For these cases, the autocorrelation basis points are placed on the lateral plane on both the main shear layer and the septum shear layer. Ellipse fits are performed on the 0.5 contour. (A lower correlation value than in the side views is used here due to the decorrelating effect of the greater laser speckle in the end-view images as compared to the side-view images.) To obtain better-resolved images near separation, detailed end-view images of segments of the shear layer were obtained. The processing for the detailed end-view images is quite similar to that for the side-view images. For the autocorrelation analysis, 11 basis points on the central column of the image are used.

III. Results and Analysis

A. Time-Averaged Schlieren Images

To better appreciate the structure of this base flow, two time-averaged schlieren images are provided in Fig. 5. These images are in the symmetry plane of the flowfield and perpendicular to this plane (lateral plane), respectively; the knife edge is horizontal in both cases. Although unsuitable for quantitative interpretation in this three-dimensional flowfield, several gross features are evident. First, expansion fans are present at the separation point at all points around the base periphery, and recompression shocks are visible on all sides of the wake near reattachment. The wake is obviously asymmetric when viewing the symmetry plane (Fig. 5a). Moreover,

there is a central division, or septum, in the lateral plane image (right central portion of Fig. 5b). The septum and the wake asymmetry are absent from images of the axisymmetric blunt-base wake. These are indications of the strongly three-dimensional nature of the current flow.

B. Example Side-View Mie Scattering Images

The convective Mach number for each imaging location where a well-defined shear layer exists is calculated from the previously obtained velocity data[17]; these values are presented in Table 2. Because this flow contains a significant velocity component perpendicular to the lateral plane at some locations,[17] the lateral-plane convective Mach number values should be considered lower bounds on M_c, particularly for the septum shear layer. These M_c values are all high enough that the large-scale structures should experience significant compressibility effects.

Detailed Mie scattering images are obtained in the lateral plane at five axial positions, A–E (Fig. 3). At positions D and E, the septum shear layer is also imaged along with the main shear layer. At position C, due to the different angle between the main shear layer and septum shear layer, a separate image is obtained of the septum. The images presented here are nominally side-view images. However, due to the significant mean velocity component perpendicular to the imaging plane at some locations,[17] particularly for the septum region, the images are actually somewhat oblique to the mean flow direction. This normal velocity component implies that there is no actual reattachment point in this plane. Hence, all discussion of lateral plane "reattachment" will refer to the apparent impingement of the main shear layer upon the septum, that is, position D in Fig. 3.

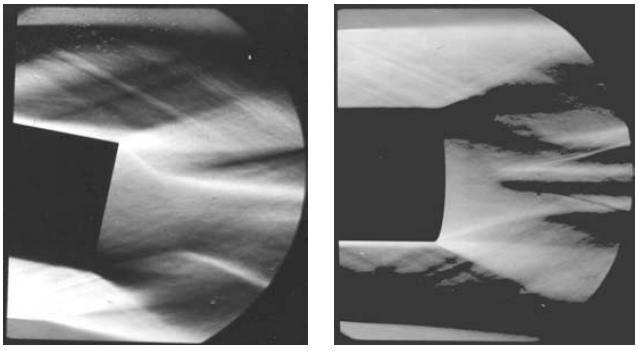

a) b)

Fig. 5 Time-averaged schlieren images: a) symmetry plane and b) lateral plane.

An example detailed image for position A is shown in the upper left of Fig. 6. As in all of the shear layer images shown, the flow direction is from left to right, with the bottom of the image toward the afterbody centerline. Several small structures are present at the interface. These structures have various shapes, but generally seem to be elliptical. The structures appear to be inclined toward the freestream flow direction, matching the results of several other studies.[1,10–12] No regular spacing of the structures is apparent, which agrees with the results in axisymmetric base flow.[12] There are many fine filaments of freestream fluid that penetrate into the recirculation fluid. In the upper left corner of the image, the expansion fan from the separation corner is faintly visible as a generally brighter region; this becomes quite obvious in the average image for this ensemble.

For position B, the shear layer is quite similar to that for position A. The shear layer is moderately thicker, and the structures appear slightly larger than at position A, though they are still relatively small. The filaments of freestream fluid that penetrate into the recirculation fluid are more obvious than at position A.

Inspection of numerous example images shows that there is typically a bright band immediately above the interface at positions A and B. This band has a distinctly different texture than the freestream, with small embedded pockets of dark fluid. A similar band has been observed previously in compressible base flow shear layers,[12] a compressible boundary layer after an expansion fan,[9] and a supersonic cavity flow shear layer.[27] It is hypothesized that this bright band contains remnants of the afterbody boundary layer fluid.[12] It is further hypothesized that the expansion process causes the boundary layer remnants to appear brighter than the freestream, as opposed to their darker appearance in the cavity flow images of Ünalmis et al.,[27] for which there is no expansion.

The most obvious feature at position C, in the recompression region, is the recompression shock that passes through the image. Recompression has a marked effect on the structures. The structures are fairly small near the left edge of the image. After recompression,

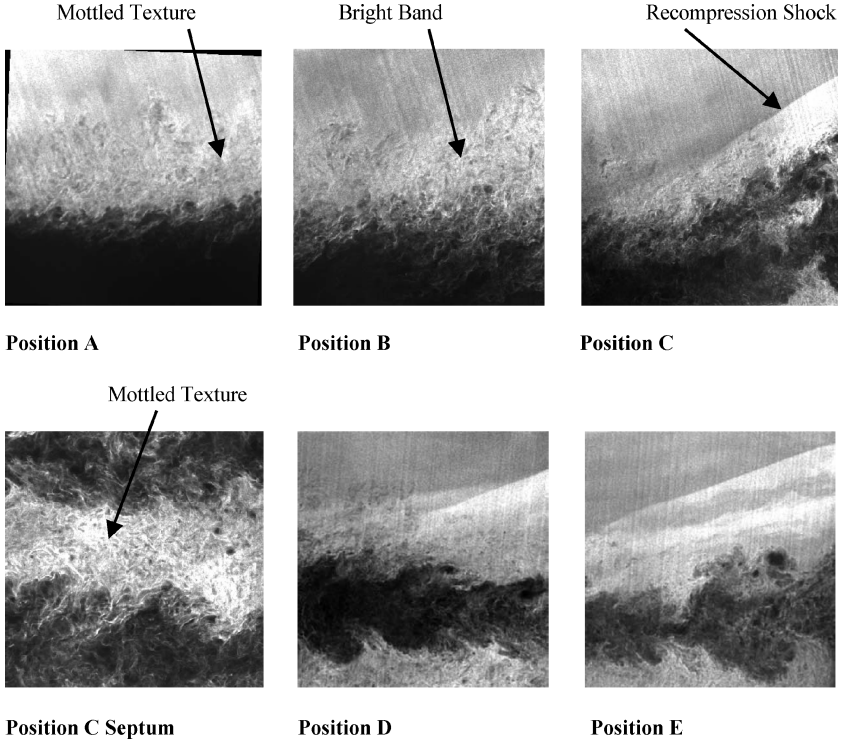

Fig. 6 Example lateral-plane Mie scattering images.

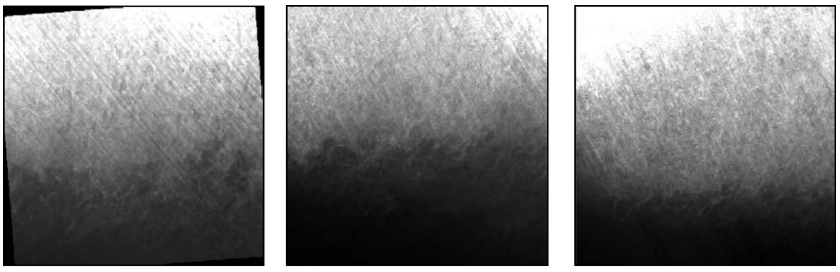

Position F **Position G** **Position H**

Fig. 7 Example leeward plane Mie scattering images.

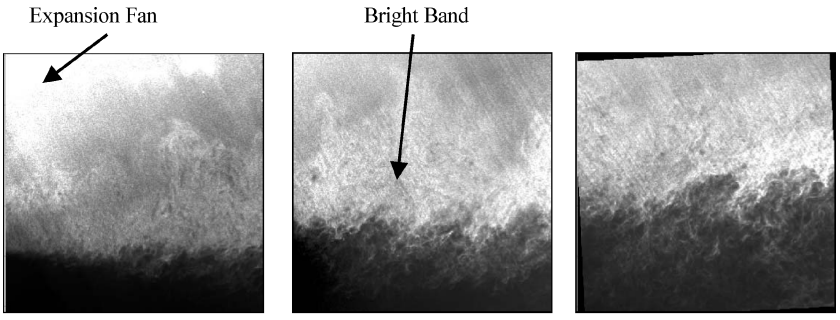

Position I **Position J** **Position K**

Fig. 8 Example windward plane Mie scattering images.

however, the structures become much larger and seemingly less well organized. Examination of the entire image ensemble shows that the recompression shock is quite variable in position and slope.

For the septum at position C, the bright region of the septum is not as uniform as the freestream for the main shear layer. In fact, the texture of this region bears a striking resemblance to the bright band above the interface at positions A and B. This suggests that the septum is made up largely of boundary-layer remnant fluid. This is an interesting result; a mechanism must be present to drive boundary-layer remnant fluid toward the wake centerline, as will be discussed further. The structures for the septum at position C are generally rather large and elliptical. Again, there appears to be no regularity in the structure spacing. The structures on each side of the septum are not matched and appear to be spaced independently; no structure symmetry across the two sides of the septum is evident.

The recompression shock is again clearly visible for position D, during apparent reattachment. Faint shocks are occasionally seen emanating from the large-scale structures when one inspects numerous example images; this is suggestive of the existence of eddy shocklets. For the main shear layer (top interface), the structures are quite large and inclined steeply toward the freestream flow direction, but are also varied in size and shape. For the septum shear layer (bottom interface), the structures appear to be better organized. The bright area in the septum still appears to be textured, as it was at position C.

Example images for position E show that the recompression shock position is quite variable across the ensemble, as at position D. The structures are quite large, but rather disorganized. The septum appears much as it did at position D, but the structures appear slightly less well organized than at position D. The septum and freestream are quite close to intermingling near the right edge of the image.

Example leeward shear layer images are given in Fig. 7. These images are distinctly different than the lateral plane images. The shear layer interface is much less distinct, and the coherent structures are much less prominent than for the lateral plane shear layer. Indeed, the lack of a distinct edge in the leeward shear layer images makes it difficult to define an outer boundary of the shear layer. Another important difference is in the boundary-layer remnants. Unlike the lateral shear layer images, where this band was relatively thin, the entire freestream of these images appears to have the mottled texture of boundary-layer remnants. Whereas the leeward boundary layer is indeed substantially thicker than the lateral plane boundary layer,[16] the presence of such a large amount of boundary-layer remnant fluid is puzzling. This is a three-dimensional effect that will be explained by the end-view images. Little change can be seen in the images as the shear layer develops in the downstream direction.

Example images in the symmetry plane for the windward shear layer are shown in Fig. 8. Overall, the image near separation (position I) appears very similar to that for the lateral plane near separation (position A; Fig. 6). The left side of the image is very close to the separation corner, and the attendant expansion fan can be seen in the upper left-hand corner of the image, just like in the lateral-plane images. The shear layer appears to be fairly linear away from the expansion fan. Coherent structures are also evident; the structures appear quite small and are somewhat rounded, without regular spacing or consistent size.

Example images further from the base surface (positions J and K) show that the windward shear layer appears to thicken substantially as it develops, with the coherent structures becoming more prominent. The large-scale structures continue to be inclined toward the freestream flow direction, but appear to become less organized downstream. These are all trends seen in previous base-flow visualizations for an axisymmetric blunt base.[12] The structures in this plane appear to develop much more quickly than in the lateral plane. The bright band above the shear layer interface remains distinct at position J but is no longer distinct at position K.

Figure 9 shows example images of the wake in the symmetry plane after reattachment at positions L and M. The windward recompression shock is perhaps the most striking feature of these images. The shock is often curved, rather than linear, and its topology changes significantly from image to image. Most of the fluid toward the centerline of the afterbody (lower part of these images) from the shock has a similar mottled texture to the boundary-layer remnants seen in the shear layer before reattachment. The appearance of such a large quantity of former boundary-layer fluid appears at first to be at odds with the available amount of boundary-layer remnant fluid seen in both the shear layer visualizations and the velocity data.[16] This is a three-dimensional effect, the cause of which will become evident in the end-view images.

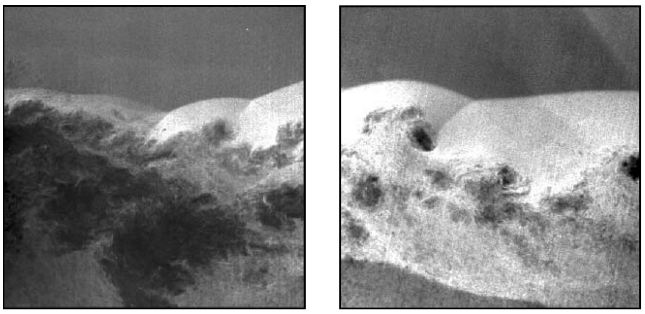

Position L Position M

Fig. 9 Example images of the symmetry plane wake and windward recompression shock.

Another feature in these images is the presence of large, dark coherent structures separated from the recirculation zone. These structures always appear behind the shock and tend to be more numerous near the reattachment point. Their complex but generally rounded appearance is reminiscent of the appearance of plan views of highly compressible shear layers.[2] There are two possible origins of these structures. Either they are the remnants of the large-scale structures from the shear layer before reattachment, or they are plan views of the structures in the septum, whose tops occasionally penetrate the laser sheet in the symmetry plane. The latter possibility is considered much more likely; further evidence will be provided by the end views.

C. Side-View Autocorrelation Statistical Results

Selected contour plots of the mean large-scale structures, as found by the autocorrelation analysis, are presented in Fig. 10 for the lateral plane. The contour lines shown are for correlation values ranging from 0.5 to 0.9 in 0.1 increments. The local average shear layer thickness is indicated for each image. Before recompression, the structures are very small relative to the local shear layer thickness and are quite elliptical. At position C, in the recompression region, the structures have grown greatly but remain elliptical. In addition, one can see that the inner contours are inclined at a greater angle to the freestream flow direction than the 0.5 contour. This effect in the recompression region has been noted by Bourdon and Dutton[12] in axisymmetric base flow and by Smith and Dutton[11] in planar base flow as well. They surmised that this occurs because the edges of the coherent structures are more sensitive to the adverse pressure gradient in the recompression region than the structure cores. After recompression (positions D and E), the structures continue to grow, but the outer contours become quite deformed, especially near the tops of the structures. Perhaps the unsteadiness of the recompression shock at these positions causes the tops of the coherent structures to deform more than the bottoms. Such deformation was not evident in visualizations of axisymmetric base flow.[12] However, the recompression shock is also not as clearly evident in those images as it is in the current visualizations.

Overall, the structures in the septum shear layer appear quite similar to the structures in the main shear layer. The direction of tilt is opposite of that for the main shear layer, however, because, for the septum, the high-speed stream is toward the bottom of the plots, whereas it is toward the top for the main shear layer. Little, if any, difference can be seen in the inclination angle of the various contours at position C in the septum, unlike at position C in the main shear layer. This is perhaps not surprising because the recompression shock is not communicated across the subsonic lobe of the wake between the main shear layer and the septum.

Contour plots for the autocorrelation calculations in the symmetry plane shear layers are given in Fig. 11, with the orientation the same as in the example images. The leeward autocorrelation contours are quite elliptical down to the 0.5 correlation contour, whereas the windward correlation contours for the lower correlation values are quite irregular. Overall, the large-scale structures are much less

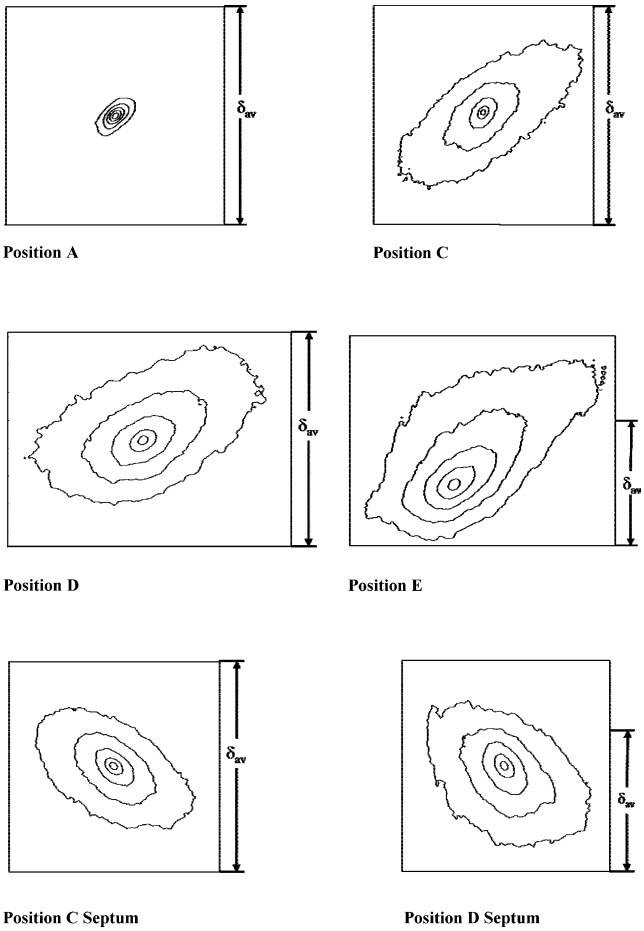

Fig. 10 Autocorrelation contour plots for the lateral plane; orientation is same as in example images.

significant on the leeward side of the shear layer, given the small size of the contours compared to the windward- or lateral-plane contours. The leeward contours also generally become smaller relative to the shear layer thickness as the shear layer develops, whereas the contours on the windward side appear to grow. These trends confirm what was seen in the example images, that is, that the dynamics of the large-scale structures in the leeward part of the shear layer are quite different from those in the windward or lateral parts.

Rotation between the outer and inner contour lines can be seen in the windward shear layer, particularly at position K. Because this position is the closest position to reattachment in the windward part of the shear layer, this suggests that an adverse pressure gradient may already be felt at position K, even though there is no evidence that the recompression shock extends this far upstream in the example images. This effect was also seen by Bourdon and Dutton[12] in their visualization of axisymmetric base flow. This could be caused by upstream communication of the recompression pressure gradient through the subsonic part of the shear layer or the recirculation region.

Figure 12 shows the autocorrelation contours for the symmetry plane images after reattachment. As expected after viewing the example Mie scattering images, the contours become more circular as the wake develops. There seems to be very little growth between the two image locations. Overall, the structures look nothing like their shear layer counterparts, casting doubt on the idea that these are remnants of symmetry plane shear layer structures that somehow survived the reattachment process.

Trends in the structure size are shown in Fig. 13, normalized by both the local shear layer thickness and the base radius. Structure size data (Figs. 13a and 13b) show that the structures are much larger on the windward side of the shear layer than in the lateral plane, whereas the structures on the leeward side of the shear layer are small

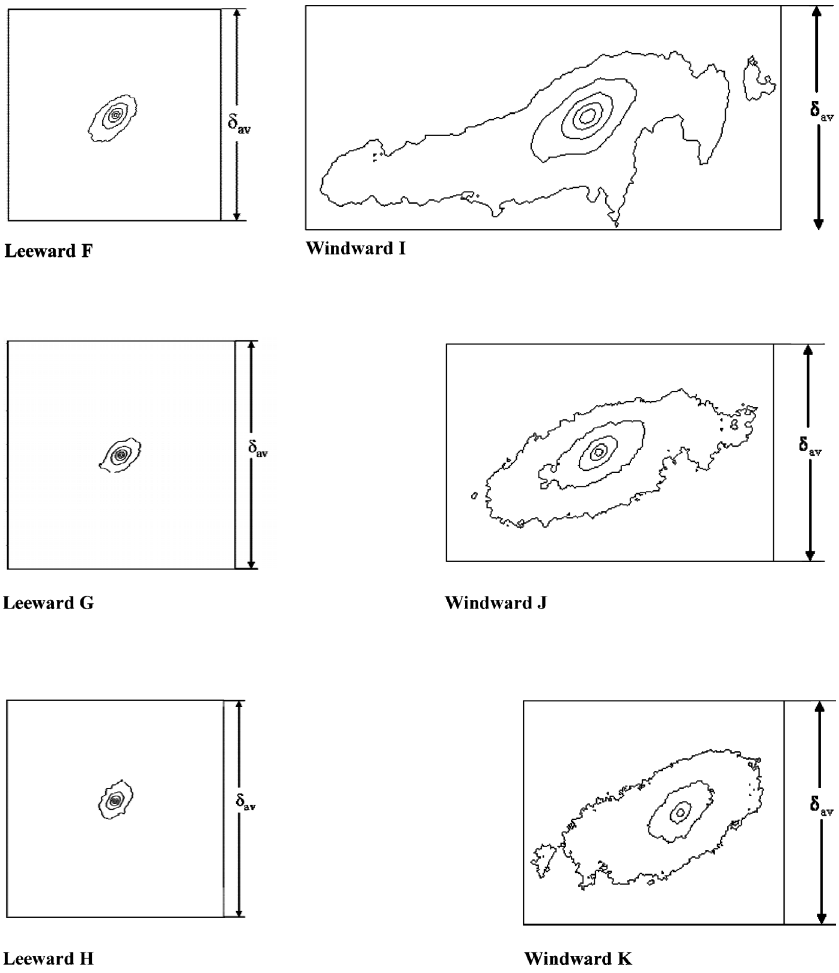

Fig. 11 Autocorrelation contours for the shear layer in the symmetry plane: correlation contours from 0.5 to 0.9 except windward K, correlation contours from 0.6 to 0.9.

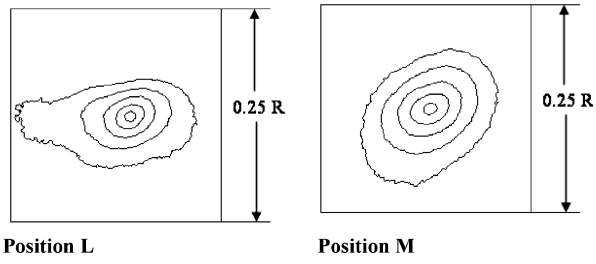

Fig. 12 Symmetry plane autocorrelation contours after reattachment: afterbody centerline horizontal, windward freestream toward the top, and mean flow left to right.

throughout its development. The general trend in the windward and lateral planes is for the structure size to increase as the shear layer develops, both in absolute terms and as a fraction of the local shear layer thickness.

The structure size trends match the behavior of axisymmetric base flow before reattachment.[12] In axisymmetric base flow, however, the structure size decreases after reattachment, although it continues to grow in this flow in the lateral plane. There are several possible reasons for this behavior. The shear layer after apparent reattachment in the current flow is confined by the septum, whereas there is no such confinement for the axisymmetric flow. Thus, the shear layer thickness, which is used to normalize the axisymmetric data, will be much different between the two flows. In the current flow, the shear layer converges in only one direction at apparent reattachment in the lateral plane, not symmetrically as is found in the axisymmetric base flow. Thus, the effects of streamline convergence would be expected to be much different between these two flows.

Trends in the structure eccentricity and inclination angle are given in Fig. 14. The eccentricity data (Fig. 14a) show little trend with downstream direction in the lateral shear layer; decrease for the leeward, septum, and wake regions as the flow develops; and increase slightly for the windward part of the shear layer as it develops. From the data for axisymmetric base flow,[12] the general trend in eccentricity seems to be for increases as the shear layer approaches reattachment, where the turbulence intensity is increases,[17,19] and decreases in areas where the turbulence becomes less intense. The trends for the windward and leeward planes of the current flow clearly follow this trend. The relatively low eccentricity values for the symmetry plane wake images after reattachment match the expected behavior for plan views of three-dimensional structures in a highly compressible shear layer, which do not have a strongly preferred orientation.

Conclusions are harder to draw from the inclination angle data (Fig. 14b). The lateral plane data appear to show a decrease in structure angle at apparent reattachment. The structures in the windward and septum areas of the shear layer seem to have decreasing structure angles as the shear layer develops, in agreement with the findings for axisymmetric base flow. The inclination angle for the leeward side of the wake has no clear trend.

D. Example Global End-View Images

Example global end-view Mie scattering images at various axial positions are shown in Fig. 15. The image locations and sizes are given in Table 3. In these images, the leeward part of the wake is at the top of the images, and flow is out of the page. Immediately after

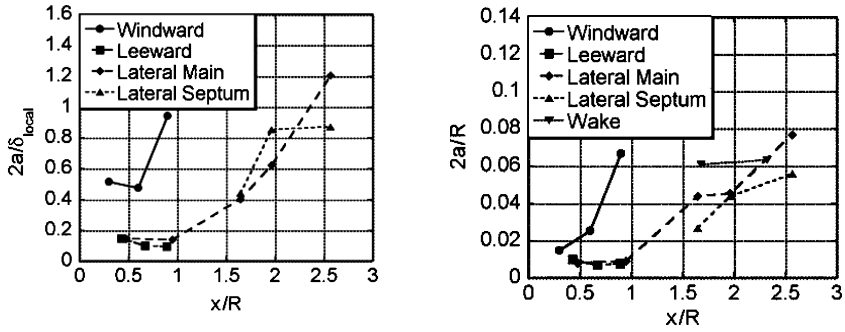

a) b)

Fig. 13 Side-view image autocorrelation contour size (major axis) normalized by a) local shear layer thickness and b) base radius.

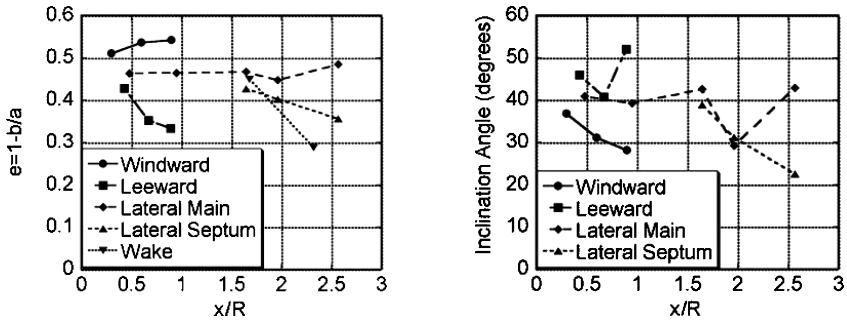

a) b)

Fig. 14 Side-view image autocorrelation statistics for the 0.6 correlation contour: a) eccentricity and b) inclination angle of the major axis with respect to the mean shear layer orientation.

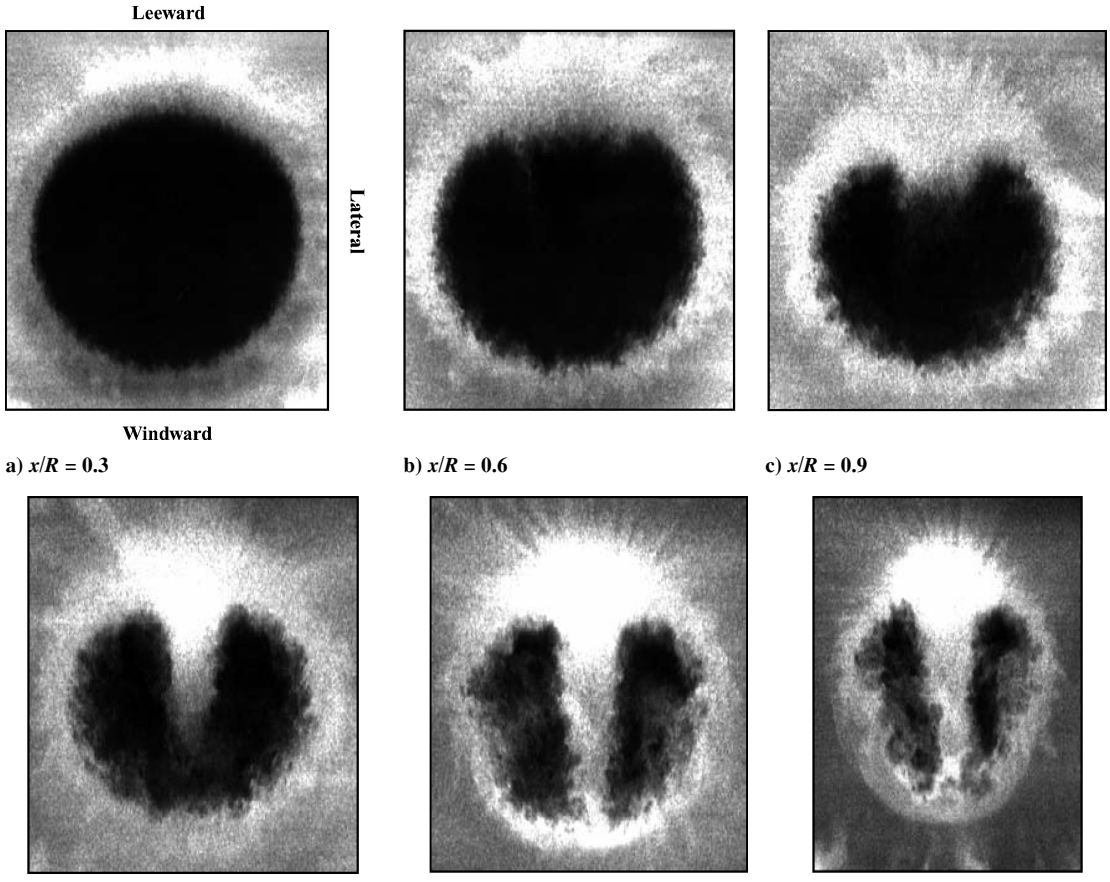

a) $x/R = 0.3$ b) $x/R = 0.6$ c) $x/R = 0.9$

d) $x/R = 1.2$ e) $x/R = 1.6$ f) $x/R = 2.0$

Fig. 15 Example global end-view Mie scattering images; width of images from 2.2*R* for $x/R = 0.3$ to 1.5*R* for $x/R = 2.0$.

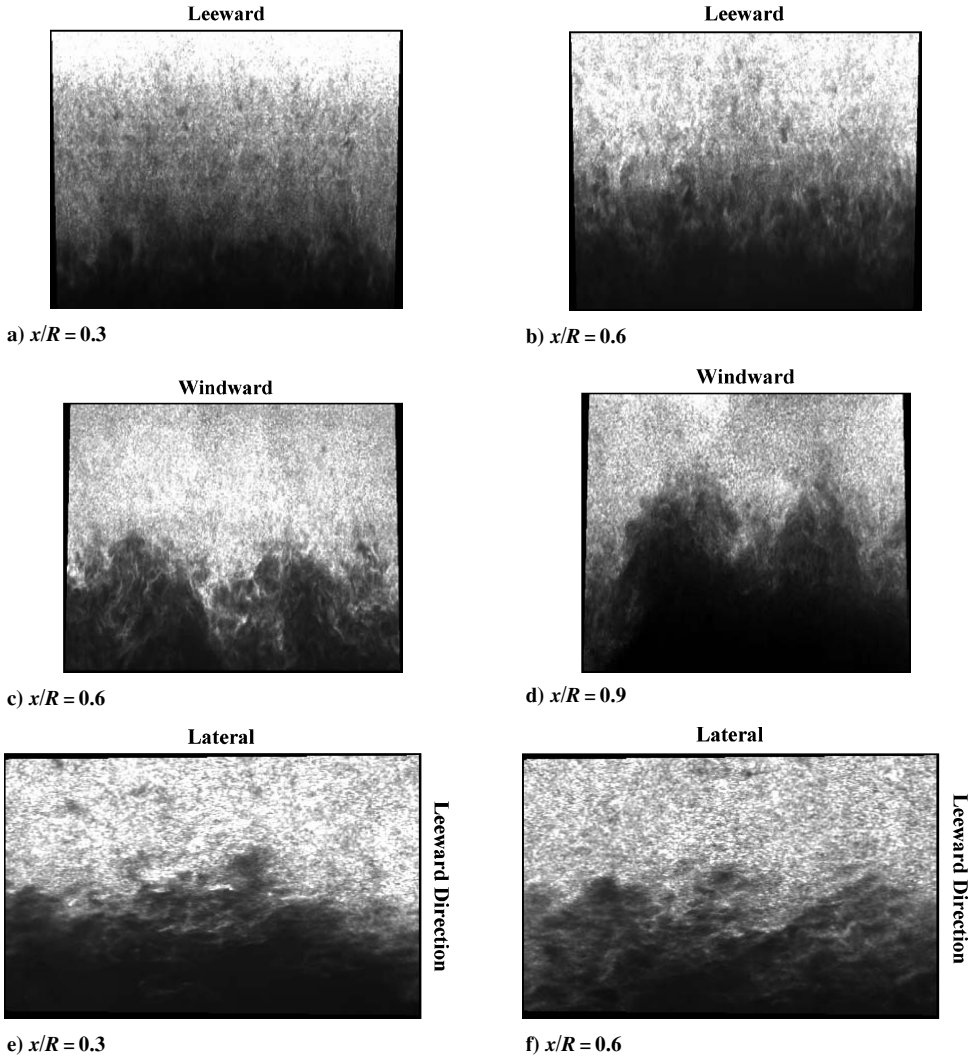

Fig. 16 Detailed Mie scattering end-view images.

separation (Fig. 15a), the recirculation region is largely circular, with small coherent structures embedded within a thin shear layer. The bright band of fluid in the shear layer described earlier is also evident in the leeward part of this image. As one moves downstream (Figs. 15b and 15c), the windward (bottom) and lateral (side) parts of the shear layer become thicker and contain large coherent structures, while converging toward the afterbody centerline. This behavior is very similar to that found in axisymmetric base flow.[12] In the leeward plane, however, the shear layer appears to grow quite differently. The high-speed side of the leeward shear layer does not appear to move toward the centerline between axial locations, while the low-speed side quickly extends toward the centerline, leading to a sharp increase in the shear layer thickness. Large-scale structures are difficult to detect on the leeward part of the symmetry plane.

At reattachment (Fig. 15d), the leeward shear layer is forming the septum that will eventually divide the wake. At this point, the septum does not extend all of the way to the windward shear layer in the Mie scattering images, even though the shear layer has reattached as determined from the velocity data.[17] This is because the region near reattachment is subsonic and, therefore, too warm to support the ethanol droplets responsible for scattering. By $x/R = 1.6$ (Fig. 15e), the velocity data[17] show that nearly the entire wake is supersonic in the symmetry plane, and the septum now completely divides the wake in two. The lateral plane still appears to evolve like axisymmetric base flow,[12] with the large-scale structures becoming larger relative to the shear layer thickness. One can also see large-scale structures in the septum shear layer, as expected from the lateral plane side-view results. After reattachment (Figs. 15e and 15f), the wake narrows much more in the lateral direction than in the symmetry plane, with the low-speed wake-core region becoming biased toward the leeward side of the shear layer. The scattered intensity begins to rise within the low-speed region, indicating that this region is beginning to accelerate, as confirmed by the velocity data in the lateral plane.[17] The structures in the septum penetrate a significant fraction of the septum thickness toward the centerline. Hence, it seems quite possible that these structures occasionally penetrate the wake centerline, perhaps explaining the coherent structures seen in the symmetry plane after reattachment (Fig. 8).

E. Example Detailed End-View Images

Whereas the global end-view images demonstrate the gross structure of the wake, the resolution of these images is inadequate to discern the details of the large-scale coherent structures in the shear layer, especially near separation. Example detailed end-view images at selected positions are shown in Fig. 16. As in the side-view images, the large-scale structures are much larger and more noticeable in the windward part of the shear layer (Figs. 16c and 16d) than in the leeward part (Figs. 16a and 16b). The structures in the windward part of the shear layer appear rounded and become more distinct between $x/R = 0.6$ (Fig. 16c) and $x/R = 0.9$ (Fig. 16d). They do not appear to be preferentially inclined in any direction. The windward plane results are very similar to those seen in axisymmetric flow. In the lateral plane (Figs. 16e and 16f), the structures are distinct, but they are smaller than in the windward part of the shear layer and appear to be inclined toward the leeward side of the wake.

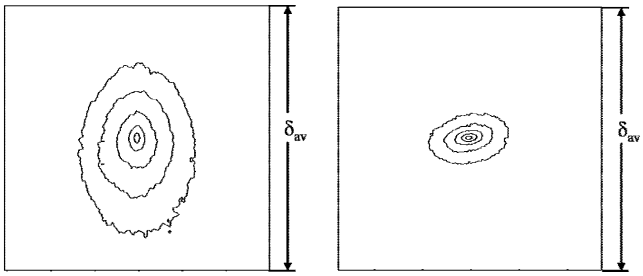

a) Windward, $x/R = 0.9$ b) Lateral, $x/R = 0.9$

Fig. 17 Example detailed end-view autocorrelation contours.

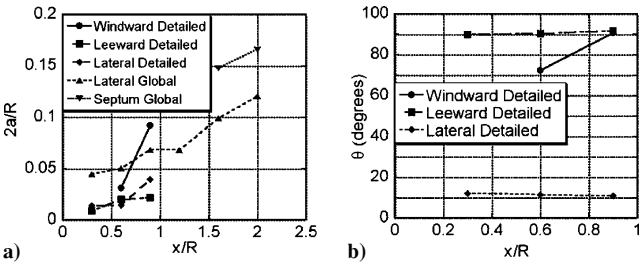

Fig. 18 End-view autocorrelation results: a) structure major axis nondimensionalized by the base radius and b) structure major axis angle from mean shear layer direction.

F. End-View Autocorrelation Analysis

Autocorrelation analysis was performed on both the global and detailed end views. Two example autocorrelation contours are shown in Fig. 17. The images are in the same orientation as the corresponding example images in Fig. 15. Both sets of contours are quite elliptical. The windward contours are largely aligned radially, whereas the lateral-plane contours are inclined toward the leeward side of the wake. The windward structures are much larger relative to the shear layer thickness than the lateral-plane structures, matching the results seen for the side-view autocorrelation analysis.

The trends in autocorrelation contour size and inclination angle with respect to the mean shear layer direction (for the 0.5 correlation contour) are shown in Fig. 18. Because the autocorrelation contour size is so small in the global views, these data for inclination angle are considered unreliable, and hence, only the data for the detailed views are plotted. Values of the structure size near separation from both the global and detailed end-view images for the lateral plane are shown to demonstrate the importance of adequate image resolution in obtaining accurate structure statistics and to make the overall trends clearer. Reflected light from the afterbody surface substantially degraded the detailed windward end-view autocorrelation data at $x/R = 0.3$, and so these data are not plotted.

The trends in end-view structure size (Fig. 18a) are quite clear. In all views, the structures tend to grow as the shear layer develops. The detailed views show smaller structure sizes than the global views, particularly close to separation. This is due to the increased resolution of the detailed views. The windward structures are significantly larger than the leeward and lateral structures in the detailed end views, which is not surprising given the appearance of the example images in Fig. 16.

The structure angle trends (Fig. 18b) show a very interesting result. The windward and leeward structures are all relatively close to being aligned radially (90 deg) with the wake. It is reasonable, because these structures are on the symmetry plane of the wake, that the average structure would be aligned with the symmetry plane. The lateral-plane structures, however, are consistently inclined at a relatively low angle (10–11 deg) with respect to the shear layer toward the leeward side of the wake. This agrees with the appearance of the example detailed end-view images for the lateral plane. These trends are also seen for the global end-view autocorrelation data for the lateral plane, although these data are not shown. There are two possible explanations. First, to correct the perspective distortion introduced by obtaining the end views at an oblique angle, the images are stretched largely in one direction. For the windward and leeward images, this stretch is radial (vertical as the images are shown in Fig. 16). For the lateral plane, on the other hand, this stretch is circumferential (horizontal in Figs. 16e and 16f). The perspective correction might be expected to distort the lateral plane autocorrelation contours, especially given the interpolation used in the distortion correction code. However, one would expect a structure angle of zero if the deformation were due to the flattening routine alone. The other possibility is that there is circumferential flow around the wake on the lateral plane. Thus, these images would be oblique and may appear reminiscent of the side-view images, with their inclined large-scale structures.

G. Discussion

The preceding data can be compiled to give a comprehensive view of the qualitative behavior of the flow. Surface-flow visualizations on the afterbody[15] and the boundary-layer velocity data[16] suggest that mass builds up on the lee side of the afterbody boundary layer before separation due to the circumferential pressure gradient around the afterbody. Given the detailed flow visualizations, it is hypothesized that this circumferential flow continues after separation. This causes mass to continue to build up on the lee side of the wake. Eventually, this mass is forced down the centerline of the wake, forming the septum. This septum increases the area for entrainment of recirculation fluid in the wake, acting to reduce the base pressure. Because of the small thickness of the septum, large-scale structures in the septum shear layer occasionally penetrate the symmetry plane of the wake, causing the large-scale structures seen in the wake in the symmetry plane. Hence, these large-scale structures are essentially plan views of the coherent structures in the septum shear layers.

Several lines of evidence support this hypothesis. First, side-view images of the leeward part of the shear layer, the symmetry plane after reattachment, and the septum show a mottled texture, much like the boundary-layer remnants in other side-view images. Hence, it seems quite likely that the septum and much of the leeward part of the shear layer are largely made up of boundary-layer remnant fluid. The inclination of the large-scale structures in the lateral-plane detailed end views suggests that there is significant circumferential flow from the windward to leeward parts of the wake, causing the large-scale structures to incline, like in the side-view images. The velocity vectors from the laser Doppler velocimetry data[17] diverge over a large region of the leeward part of the wake without gross acceleration; this hypothesis explains this behavior. This also explains how the leeward shear layer can become so thick without significant action by large-scale coherent structures, which are generally deemed critical in the dynamics of shear layer growth.

The behavior of the wake can also be interpreted by thinking of the afterbody as a lifting body. The pressure gradient across the afterbody will produce a lift force. Because the production of lift by inviscid mechanisms requires the presence of circulation, lifting bodies produce vortex wakes by their very nature. This may help explain the two-lobed vortex wake produced by the current afterbody.

IV. Conclusions

Extensive flow visualizations of a blunt-base cylinder at 10-deg angle of attack have been performed using planar Mie scattering imaging. Large-scale structures are quite evident in the flow visualizations of the windward and lateral parts of the shear layer, but not for the leeward part. Autocorrelation analysis shows that the average structures are largely elliptical and inclined toward the freestream direction for all side-view images. The shear layer structures grow as the shear layer develops in the windward and lateral planes, but not in the leeward plane, with the greatest average structure size in the windward plane. As the wake develops toward reattachment, a septum of high-speed fluid is driven from the leeward part of the shear layer across the wake centerline toward the windward side of the wake, dividing the wake into two lobes of low-speed fluid after reattachment. End-view visualizations confirm that the large-scale structures are much more obvious on the windward

and lateral planes than on the leeward plane before reattachment. The largest end-view structures are found in the windward plane of the shear layer. End-view images of the lateral plane structures are inclined toward the leeward side of the wake. Overall, the data suggest that circumferential flow from windward to leeward occurs in the wake after separation, causing a buildup of fluid on the leeward part of the wake. This buildup is forced down the symmetry plane from leeward to windward, causing the short reattachment length and low base pressure for this body compared to that for axisymmetric flow.

Acknowledgments

This work was supported by the U.S. Army Research Office, Grant DAAD19-01-1-0367, with Thomas Doligalski as Technical Monitor.

References

[1]Papamoschou, D., and Bunyajitradulya, A., "Evolution of Large Eddies in Compressible Shear Layers," *Physics of Fluids*, Vol. 9, No. 3, 1997, pp. 756–765.

[2]Clemens, N., and Mungal, M., "Large-Scale Structure and Entrainment in the Supersonic Mixing Layer," *Journal of Fluid Mechanics*, Vol. 284, Feb. 1995, pp. 171–216.

[3]Goebel, S., and Dutton, J., "Experimental Study of Compressible Turbulent Mixing Layers," *AIAA Journal*, Vol. 29, No. 4, 1991, pp. 538–546.

[4]Elliott, G., and Samimy, M., "Compressibility Effects in Free Shear Layers," *Physics of Fluids A*, Vol. 2, No. 7, 1990, pp. 1231–1240.

[5]Bernal, L., and Roshko, A., "Streamwise Vortex Structure in Plane Mixing Layers," *Journal of Fluid Mechanics*, Vol. 170, 1986, pp. 499–525.

[6]Dimotakis, P., "Two-Dimensional Shear-Layer Entrainment," *AIAA Journal*, Vol. 24, No. 11, 1986, pp. 1791–1796.

[7]Bradshaw, P., "The Effect of Mean Compression or Dilatation on the Turbulence Structure of Supersonic Boundary Layers," *Journal of Fluid Mechanics*, Vol. 63, No. 3, 1974, pp. 449–464.

[8]Bowersox, R., Wier, R., Glawe, D., and Gogineni, S., "Measurements of Turbulent Flow Structure in Supersonic Curved Wall Boundary Layers," *Journal of Propulsion and Power*, Vol. 16, No. 1, 2000, pp. 153, 154.

[9]Arnette, S., Samimy, M., and Elliott, G., "The Effects of Expansion on the Turbulence Structure of Compressible Boundary Layers," *Journal of Fluid Mechanics*, Vol. 367, 1998, pp. 67–105.

[10]Ramaswamy, M., Loth, E., and Dutton, J., "Free Shear Layer Interaction with an Expansion–Compression Wave Pair," *AIAA Journal*, Vol. 34, No. 3, 1996, pp. 565–571.

[11]Smith, K., and Dutton, J., "Investigation of Large-Scale Structures in Supersonic Planar Base Flows," *AIAA Journal*, Vol. 34, No. 6, 1996, pp. 1146–1152.

[12]Bourdon, C., and Dutton, J., "Planar Visualizations of Large-Scale Turbulent Structures in Axisymmetric Supersonic Separated Flows," *Physics of Fluids*, Vol. 11, No. 1, 1999, pp. 201–213.

[13]Poggie, J., and Smits, A. J., "Large-Scale Coherent Turbulence Structures in a Compressible Mixing Layer Flow," AIAA Paper 96-0440, 1996.

[14]Scarano, F., and van Oudheusden, B., "Planar Velocity Measurements of a Two-Dimensional Compressible Wake," *Experiments in Fluids*, Vol. 34, No. 3, 2003, pp. 430–441.

[15]Boswell, B., and Dutton, J., "Flow Visualizations and Measurements of a Three-Dimensional Supersonic Separated Flow," *AIAA Journal*, Vol. 39, No. 1, 2001, pp. 113–121.

[16]Boswell, B., and Dutton, J., "Velocity Measurements in a Pressure-Driven Three-Dimensional Compressible Turbulent Boundary Layer," *AIAA Journal*, Vol. 40, No. 7, 2002, pp. 1300–1310.

[17]Boswell, B., and Dutton, J., "Velocity Measurements in a Three-Dimensional Compressible Base Flow," *AIAA Journal*, Vol. 41, No. 5, 2003, pp. 785–794.

[18]Dayman, B., "Support Interference Effects on the Supersonic Wake," *AIAA Journal*, Vol. 1, No. 8, 1963, pp. 1921–1923.

[19]Herrin, J., and Dutton, J., "Supersonic Base Flow Experiments in the Near Wake of a Cylindrical Afterbody," *AIAA Journal*, Vol. 32, No. 1, 1994, pp. 77–83.

[20]Clemens, N., and Mungal, M., "A Planar Mie Scattering Technique for Visualizing Supersonic Mixing Flows," *Experiments in Fluids*, Vol. 11, No. 2/3, 1991, pp. 175–185.

[21]Samimy, M., and Lele, S., "Motion of Particles with Inertia in a Compressible Free Shear Layer," *Physics of Fluids A*, Vol. 3, No. 8, 1991, pp. 1915–1923.

[22]Wegener, P., Clumpner, J., and Wu, B., "Homogeneous Nucleation and Growth of Ethanol Droplets in Supersonic Flow," *Physics of Fluids*, Vol. 15, No. 11, 1972, pp. 1869–1876.

[23]Elliott, G., and Beutner, T., "Molecular Filter Based Planar Doppler Velocimetry," *Progress in Aerospace Sciences*, Vol. 35, No. 8, 1999, pp. 799–845.

[24]Smith, M., "The Reduction of Laser Speckle Noise in Planar Doppler Velocimetry Systems," AIAA Paper 98-2607, 1998.

[25]Miles, R., and Lempert, W., "Two-Dimensional Measurement of Density, Velocity, and Temperature in Turbulent High-Speed Air Flows by UV Rayleigh Scattering," *Applied Physics B*, Vol. 51, No. 1, 1990, pp. 1–7.

[26]Halíř, R., and Flusser, J., "Numerically Stable Direct Least Squares Fitting of Ellipses," *Proceedings of the 6th International Conference in Central Europe on Computer Graphics and Visualization*, WSCG '98, Univ. of West Bohemia, Plzen, Czech Republic, 1998, pp. 125–132.

[27]Ünalmis, Ö., Clemens, N., and Dolling, D., "Experimental Study of Shear-Layer/Acoustics Coupling in Mach 5 Cavity Flow," *AIAA Journal*, Vol. 39, No. 2, 2001, pp. 242–252.

W. Dahm
Associate Editor